Article

# Localization of Nonblinking Point Sources Using Higher-Order-Mode Detection and Optical Heterodyning: Developing a Strategy for Extending the Scope of Molecular, Super-resolution Imaging

Kalyan Santra, Viet Nguyen, Emily A. Smith, Jacob W. Petrich,* and Xueyu Song*

ACCESS | Metrics & More | Article Recommendations | Supporting Information

**ABSTRACT:** While the stochastic, "blinking" nature of fluorescent systems has enabled the super-resolution of their localization by the fitting of their point-spread functions (PSFs), this strategy cannot be exploited for similar resolution of "nonblinking" systems, such as those that might be encountered in a coherent Raman experiment. An alternative method for subdiffraction-limited imaging lies in the exploitation of optical heterodyning. For example, if a Gaussian PSF (a TEM00 mode) of a point emitter is displaced with respect to the origin of the optical system, photons in the higher-order TEM modes carry information about that displacement. Information concerning the displacement can be extracted from photons in these higher-order modes. These photons can be collected by optical heterodyning, which exploits the large gain in a detector's response to an optical signal from an emitter coupled to a local oscillator, which is prepared in the TEM of interest, e.g., TEM10. We have generalized and developed the heterodyning technique to localize point emitters via the detection of higher-order spatial modes. We have developed a theoretical approach to find a practical estimation limit of the localization parameters using a realistic model that accounts for shot noise, background noise, and Gaussian noise. To demonstrate the applicability of the method, we designed experiments in which a laser is a surrogate for one and two point emitters. Using the Fisher information and its accompanying Cramér-Rao lower bound, we demonstrate super-resolution localization in these cases: we show that objects can be localized to roughly 2−3 orders of magnitude of their point-spread function's size for a given optical system. Finally and most importantly, it is suggested that the results will ultimately be generalizable to multiple emitters and, most importantly, to "nonblinking" molecular systems, which will be essential for broadening the scope of super-resolution measurements beyond the limits of fluorescence-based techniques.
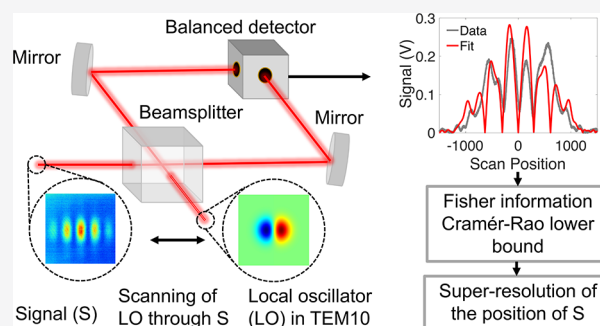
## INTRODUCTION

The diffraction of light determines the limit of the spatial resolution of optical imaging. This "diffraction limit" is traditionally given by Rayleigh's or Abbe's diffraction criterion. Rayleigh's criterion states that the separation between two equally bright point sources cannot be determined to a distance smaller than $1.22\lambda/2NA$; Abbe's, $\lambda/2NA$. $\lambda$ is the wavelength of light, and NA is the numerical aperture of the objective lens. Over the past few decades, various techniques, such as simulated emission depletion (STED),[1−3] stochastic optical reconstruction microscopy (STORM),[4,5] photoactivated localization microscopy (PALM),[6−8] structured illumination microscopy (SIM),[9,10] and their variants, have been developed to circumvent the diffraction limit. Several super-resolution techniques (such as STORM and PALM) rely on the stochastic ("blinking") nature of the physical process of fluorescence: each fluorophore is activated independently to avoid overlap in its detection, and a series of images are captured by a high-speed camera.

In these types of experiments, spatial localization is obtained by fitting the observed photon distribution on the image plane with an appropriate point-spread function (PSF). The precision in the estimation of the position of point sources can be formulated in terms of the Fisher information (FI) and the associated Cramér-Rao lower bound (CRLB), which set well-defined limits on it. These techniques can provide subdiffraction-limited spatial resolution down to a few nanometers. Their tremendous success, however, depends on the presence of fluorophores that provide the required stochastic process. Often, the sample of interest does not contain a native fluorophore. In these cases, one must resort either to labeling of the sample with exogenous fluorophores or

to modifying endogenous molecules, for example, genetic modification of proteins. In addition to the difficulty (or impossibility) of labeling samples, the cytotoxic effects of these probes and their photobleaching pose serious limitations on the scope of these techniques. Thus, vibrational imaging techniques like coherent anti-Stokes Raman scattering (CARS)[11−13] and stimulated Raman scattering (SRS)[14,15] provide the advantage of enabling label-free imaging of biological samples. The coherent Raman techniques, however, have their own limitations. They typically are used at wavelengths longer than those that are employed in fluorescence measurements, and the longer wavelengths diminish the spatial resolution, in accord with the Rayleigh and Abbe limits. Most importantly, the nonblinking character of Raman signals renders them unamenable to the super-resolution techniques for fluorescence signals that are listed above. Several attempts[16−25] have been made to improve the spatial resolution in vibrational imaging. These include STED-like approaches[19,21,23] and exploiting the nonlinear saturation of the population difference of vibrational states at high laser intensities.[25,26] We have observed that given the high laser intensities required for saturated CARS measurements and the propensity for sample damage, an improvement of a factor of "only" ∼2 could be achieved for the spatial and spectral resolution, with respect to the diffraction limit.[26] We concluded that improvements in the spatial resolution of nonblinking probes must be accompanied not only by a novel experimental design but also by novel methods of data analysis.

The number of photons collected limits the precision of the localization of an isolated emitter.[27,28] Ober and co-workers[29,30] have pointed out that for two emitters, the precision with which they are separated is fundamentally limited by the convergence of the Fisher information to zero when the two point sources become sufficiently close. Tsang and co-workers have shown, via both quantum and semiclassical treatments, that the maximum Fisher information that can be extracted remains relatively constant at any separation.[31−33] They showed that the electromagnetic field from the two emitters can be expressed in terms of the complete orthonormal basis, for example, the Hermite−Gaussian basis [i.e., the transverse electromagnetic modes (TEMs)]. To determine the maximum Fisher information, the true waveform of the electromagnetic field of the emitters must be determined. This, in principle, requires that photons from all of the TEM modes of the emitter be collected separately. Clearly, it is impossible to isolate all TEM modes. It is possible, however, to capture enough photons from enough higher-order modes to improve the precision of the estimation. Several techniques have been developed on the basis of this principle.[34−37] It has been shown experimentally that the use of TEM10 by itself can provide a better estimation of the separation in the small-distance regime.[37,38] For example, consider a point emitter, and let us assume that its PSF is Gaussian, i.e., TEM00. If the PSF is displaced with respect to the origin of the optical system, photons in the higher-order TEM modes carry information about that displacement. If photons in these higher-order TEM modes are collected, a displacement parameter can be extracted. Direct implementation of this strategy requires a technique to extract the contribution of the higher-order modes from the electromagnetic field of the emitter. The heterodyning technique has been used for this purpose by exploiting the large gain in a detector's response to an optical signal from the emitter coupling to the mode of a local oscillator, which is prepared in the TEM of interest, e.g., TEM10.[37,39] The mixing of the signal field with the local oscillator field in TEM10 carries information regarding the localization parameters of the emitter, or emitters.

Motivated by the scope of the heterodyning technique, in this study we have generalized it to localize nonblinking, point emitters via the detection of higher-order spatial modes. We have developed a theoretical approach to find a practical estimation limit of the localization parameters using a realistic model that accounts for shot noise, background noise, and Gaussian noise. To demonstrate the applicability of the method, we designed an experiment in which a laser is a surrogate for a point source emitter. Using the Fisher information and its accompanying Cramér-Rao lower bound, we demonstrate super-resolution localization of one and two nonblinking point emitters. The results can be generalized to multiple point emitters and, most importantly, to molecular systems. The outline of this paper is the following. First, we briefly outline the theoretical basis of the heterodyning method and how it is used to obtain spatial localization in mathematical terms. Specifically, we discuss the modeling of one and two point emitters, the local oscillator, and the generation of photoelectrons in the heterodyning experiment. We then briefly discuss classical estimation theory and the fundamental role of the Cramér-Rao lower bound and the Fisher information for the unbiased estimation of spatial localization. Second, we describe the experimental apparatus for using the TEM10 mode and optical heterodyning to obtain super-resolution localization of one and two point emitters. Finally, we discuss our results in the context of providing a robust approach to achieving super-resolution localization of molecular emitters.

## ■ THEORETICAL APPROACH TO THE HETERODYNING TECHNIQUE AND ITS USE FOR SPATIAL LOCALIZATION

**Heterodyned Signal.** Optical heterodyning is an inter-ferometric method, in which an optical signal (S) from a source of interest is mixed at a 50:50 beam splitter (BS) with a high-intensity, reference source, commonly known as the local oscillator (LO). This is accomplished with a Mach−Zehnder interferometer, whose fundamental features are illustrated in Figure 1. The electric fields of a displaced S and of a LO, prepared in a higher-order TEM mode, are superimposed and equally divided at a beam splitter. Reflection of one of the fields at the beam splitter induces a $\pi$ phase shift. The intensities of the two superimposed beams are monitored with matched square-law detectors (e.g., photodiodes). The optical frequencies of the S and LO are different in a heterodyned detection scheme: application of an acoustic−optic modulator (AOM) to one field induces a slight frequency difference between the S and LO fields, which is detected by frequency demodulation with a lock-in amplifier.

Let $E_S$ and $E_{LO}$ be the electric fields of S and LO, respectively. Classically, under the paraxial approximation, they are

$$E_S(x, y, t) = |E_S(x, y)| \exp[i(kz_S - \omega_S t + \phi_S)]$$

$$E_{LO}(x, y, t) = |E_{LO}(x, y)| \exp[i(kz_{LO} - \omega_{LO} t + \phi_{LO})]$$

$$(1)$$

$|E(x, y)|$ is the amplitude of the two fields in the transverse plane. $k$, $z$, $\omega$, $t$, and $\phi$ are the wavevector along the $z$-direction,
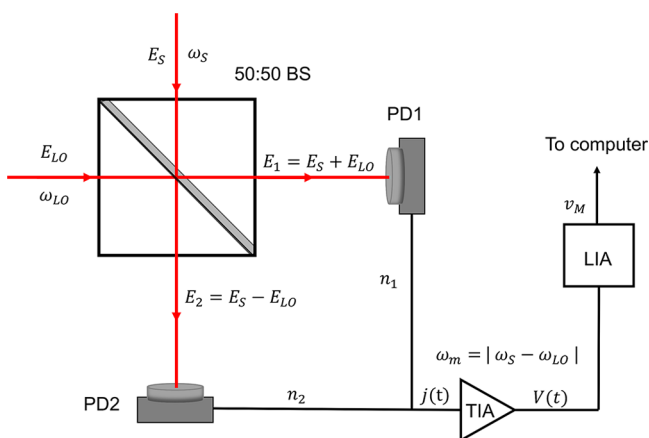
**Figure 1.** Schematic of a portion of the heterodyned detection experiment using two identical photodiodes (PD1 and PD2) and a 50:50 beam splitter (BS). The electric field of the signal ($E_s$) is mixed at the BS with the electric field of the local oscillator ($E_{LO}$). The resulting fields, $E_1$ and $E_2$, are monitored by two photodiodes whose photocurrent, $j(t)$, due to the difference in the number of the photoelectrons generated at the two detectors ($n_1$ and $n_2$), is converted to a voltage, $V(t)$, by a transimpedance amplifier (TIA). Here, the optical frequencies of S and LO are $\omega_S$ and $\omega_{LO}$, respectively. The balanced signal ($j$ or $V$) is thus modulated at the beat frequency, $\omega_m = |\omega_S - \omega_{LO}|$. The balanced signal is then demodulated at the lock-in amplifier (LIA) to obtain the demodulated signal amplitude, $v_M$.

the propagation distance along the $z$-axis, the optical frequency, the time, and the phase, respectively. $E_1$ and $E_2$ are the two output fields from the beam splitter. For a lossless 50:50 beam splitter, we have[40,41]

$$E_i(x, y, t) = \frac{1}{\sqrt{2}}[E_S(x, y, t) \pm E_{LO}(x, y, t)] \tag{2}$$

where $i = 1$ or $2$. The positive sign corresponds to $E_1$, and the negative sign to $E_2$.

In balanced detection, the two output beams are incident upon two identical photodiodes, and the resultant photocurrent due to the difference in the number of the generated photoelectrons is monitored. The intensities of the superimposed beams at the photodiodes are (for $i = 1$ and $2$):

$$I_i(x, y, t) \propto |E_i(x, y, t)|^2 \tag{3}$$

Therefore, we obtain

$$I_i(x, y, t) \propto \frac{1}{2}\{|E_S(x, y)|^2 + |E_{LO}(x, y)|^2 \pm 2|E_S(x, y)|$$
$$|E_{LO}(x, y)| \cos[k(z_S - z_{LO}) - t(\omega_S - \omega_{LO})$$
$$+ (\phi_S - \phi_{LO})]\} \tag{4}$$

The positive sign corresponds to $I_1(x, y, t)$, and the negative sign to $I_2(x, y, t)$. The number of photoelectrons ($n_i$) generated in each detector is proportional to the number of photons ($N_i$) of the corresponding superimposed light, which is also proportional to the integrated intensity of the incident light across the detector area. Therefore, we have

$$n_i(t) \propto N_i(t) \propto \iint I_i(x, y, t) \, dx \, dy \tag{5}$$

The net photocurrent in the balanced detector is

$$j(t) \propto n_1(t) - n_2(t) \propto \iint [I_1(x, y, t) - I_2(x, y, t)] \, dx \, dy$$
$$= 2 \iint |E_S(x, y)||E_{LO}(x, y)|$$
$$\cos[k(z_S - z_{LO}) - t(\omega_S - \omega_{LO}) + (\phi_S - \phi_{LO})] \, dx \, dy \tag{6}$$

For a given, fixed configuration of the experiment, the constant phase factor of the modulated signal is $\phi_m = -[k(z_S - z_{LO}) + (\phi_S - \phi_{LO})]$. The balanced photocurrent, modulated at the difference frequency $\omega_m = |\omega_S - \omega_{LO}|$, using the definition of the phase given above and the fact that cosine is an even function, is

$$j(t) \propto \iint 2|E_S(x, y)||E_{LO}(x, y)| \cos(\omega_m t + \phi_m) \, dx \, dy \tag{7}$$

The balanced detector converts the photocurrent into a voltage via a transimpedance amplifier:

$$V(t) = RGj(t)$$
$$\propto \iint 2|E_S(x, y)||E_{LO}(x, y)| \cos(\omega_m t + \phi_m) \, dx \, dy \tag{8}$$

where $R$ is the resistance of the electronic circuit and $G$ the gain factor ($10^3 - 10^7$ V/A). The voltage signal is measured by the lock-in amplifier, which demodulates the signal $V(t)$ at the reference frequency $\omega_m$ set by an AOM. It is clear from eq 8 that the demodulated signal amplitude ($v$) is given by

$$v = \kappa \iint 2|E_S(x, y)||E_{LO}(x, y)| \, dx \, dy \tag{9}$$

where $\kappa$ is the proportionality constant representing responsivity (resistance, efficiency) and the gain factor of the transimpedance amplifier, and the conversion factor involving the lock-in amplifier. The constant phase factor $\phi_m$ can be set to zero by changing the phase of the reference at the demodulator in the lock-in amplifier.

**Maximum Likelihood Estimation, Noise Model, and Cramér-Rao Lower Bound.** In the heterodyning experiment, the demodulated voltage signal is measured (for more detail, see Experimental Methods) by scanning the local oscillator field with respect to the origin of the coordinate system fixed for the experimental setup in the lateral direction. We chose the horizontal $x$-direction for our proof-of-concept experiment, but the results can be generalized in both $x$- and $y$-directions. We represent these lateral shifts of the $E_{LO}$ as the scanning parameter $\mathbf{d} = (d_1, d_2, ..., d_K)$ for many discrete points in the experiment. The measured demodulated signal amplitude at a given separation $d_k$ is represented by $v_M(d_k)$. The experimental data obtained in this manner can be fitted to a suitable model for the demodulated signal amplitude represented by $v(d_k|\boldsymbol{\theta})$, where $\boldsymbol{\theta} = (\theta_1, \theta_2, ..., \theta_p)$ are the parameters describing the model. Furthermore, the experimental data are always accompanied by noise. It is, therefore, convenient to express the measured demodulated signal in terms of the realization of a random variable associated with a probability distribution of the noise governing the observable quantity (i.e., the demodulated signal amplitude). If $\mathcal{V}_M(d_k)$ represents the random variable for the observable quantity at $d_k$ and $\mathcal{N}(d_k)$ represents the corresponding noise model of the measurement system, we can write

$$\mathcal{V}_M(d_k) = v(d_k|\boldsymbol{\theta}) + \mathcal{N}(d_k) \tag{10}$$

For the sake of simplicity, we assume that all of the noise can be consolidated to a single, random variable, which has a Gaussian distribution characterized by the mean, $\mu_k$, and the variance $\sigma_k^2$; i.e., $\mathcal{N}(d_k) = \mathcal{G}(d_k|\mu_k, \sigma_k^2)$. In most cases (in which a large number of realizations is obtained), this approximation is reasonable. We, however, note that the strategy is generic and can be easily adapted for other scenarios, where a precise knowledge of each source contributing to the overall noise is known. One such treatment is presented in section C of the Supporting Information. Under this assumption, the probability distribution of the realization $v_M(d_k)$ for the given model described by its parameters, $\boldsymbol{\theta}$, can be written as

$$P_{\mathcal{G}}[v_M(d_k)|\boldsymbol{\theta}] = P_{\mathcal{G}}[v_M(d_k) - v(d_k|\boldsymbol{\theta})]$$

$$= \frac{1}{\sqrt{2\pi\sigma_k^2}} \exp\left\{-\frac{[v_M(d_k) - v(d_k|\boldsymbol{\theta}) - \mu_k]^2}{2\sigma_k^2}\right\} \tag{11}$$

From the probability distribution, one can obtain the likelihood function of the experimental measurement spanning the entire scanning range given by the independent variable, $\mathbf{d} = (d_1, d_2, ..., d_K)$, as shown in eq 12. The log-likelihood function (which is a function of the model parameters, $\boldsymbol{\theta}$) for this case is given by

$$\mathcal{L}[\boldsymbol{\theta}|v_M(d_1), v_M(d_2), ..., v_M(d_K)] = \sum_{k=1}^{K} \ln P_{\mathcal{G}}[v_M(d_k)|\boldsymbol{\theta}] \tag{12}$$

To estimate the parameters of interest, the log-likelihood function is maximized with respect to the parameters. This can be accomplished by solving the following equations analytically (if feasible)

$$\frac{\partial \mathcal{L}}{\partial \theta_p} = 0, \text{ for all } p = 1, 2, ... \tag{13}$$

or maximizing the log-likelihood itself numerically. This is known as the maximum likelihood estimation (MLE).[29,42] We can fit the data for the entire scanning range using the likelihood function given in eq 12 to obtain the estimate of the parameters and the error associated with them.

The magnitude of the error can also be estimated, analytically in certain cases, via the calculation of the Cramér-Rao lower bound (CRLB), which sets a lower bound on the variance of any unbiased estimator of a parameter of a probability distribution. Calculation of the CRLB requires a statistical description of the random variable representing the observed data from which the parameter of interest is estimated using its Fisher information (FI). The FI is the maximum amount of information that can be obtained from the random variable about the parameter of interest describing its probability distribution. Given the probability distribution, $P_{\mathcal{G}}[v_M(d_k)|\boldsymbol{\theta}]$, that the outcome of a single measurement, $v_M(d_k)$, belongs to the model with parameter $\boldsymbol{\theta}$, the CRLB[29,30,42,43] is

$$\text{cov}_{pq}(\boldsymbol{\theta}, d_k) \geq [\text{FI}(\boldsymbol{\theta}, d_k)^{-1}]_{pq} \tag{14}$$

where $\text{cov}_{pq}(\boldsymbol{\theta}, d_k)$ is the $pq$ component of the covariance matrix for the unbiased estimators, $\boldsymbol{\theta}$. FI (which is a function of both $\boldsymbol{\theta}$ and $d_k$), for a single experiment, is given by

$$[\text{FI}(\theta, d_k)]_{pq} = \mathbb{E}\left(\left\{\frac{\partial}{\partial \theta_p} \log P_{\mathcal{G}}[v_M(d_k)|\theta]\right\} \times \left\{\frac{\partial}{\partial \theta_q} \log P_{\mathcal{G}}[v_M(d_k)|\theta]\right\}\right) \tag{15}$$

where $\mathbb{E}(x)$ is the expectation value. For a single-parameter case (i.e., for $\theta$) and a case in which the observable has a continuous value, as in the case of $v_M(d_k)$, one can transform eqs 14 and 15, respectively, as follows:

$$\text{var}(\theta, d_k) \equiv \Delta^2\theta(d_k) \geq \frac{1}{\text{FI}(\theta, d_k)} \tag{16}$$

and

$$\text{FI}(\theta, d_k) = \int_{-\infty}^{+\infty} \frac{1}{P_{\mathcal{G}}[v_M(d_k)|\theta]}\left\{\frac{\partial P_{\mathcal{G}}[v_M(d_k)|\theta]}{\partial \theta}\right\}^2 dv_M(d_k) \tag{17}$$

where $\text{var}(\theta, d_k) \equiv \Delta^2\theta(d_k)$ is the variance of the unbiased estimator, $\theta$. Using the expression $P_{\mathcal{G}}[v_M(d_k|\theta)]$ from eq 11, we have

$$\text{FI}(\theta, d_k) = \frac{1}{\sigma_k^2}\left\{\frac{d[v(d_k|\theta)]}{d\theta}\right\}^2 \tag{18}$$

For the measurements of the entire range of the scanning, the total Fisher information can be obtained from the discrete sum of the Fisher information for those individual point measurements, as shown in eq 19.

$$\text{FI}_T(\theta) = \sum_{k=1}^{K} \frac{1}{\sigma_k^2}\left\{\frac{d[v(d_k|\theta)]}{d\theta}\right\}^2 \Delta d \tag{19}$$

where $\Delta d$ is the step size of the scan. The expression for the variance can be obtained by using the total Fisher information in eq 16.

The theoretical models developed in this section are used to predict the maximum accuracy of the estimating parameters of interest by calculating the errors associated with the estimation analytically and numerically via the computation of the Fisher information and the maximum likelihood. All numerical calculation, simulations, and fitting of the experimental data were performed in MATLAB.

**Modeling a Single Emitter and the Local Oscillator Using a Hermite–Gaussian-Mode Approximation.** In a typical imaging experiment, the light field from the source in the object plane passes through the collection optics, comprised of an objective lens and other assorted elements. If this light originates from a single point source, its field has a characteristic response function at the image plane, better known as the PSF. In the Hermite-Gaussian-mode approximation, we assume that the PSF can be represented by a TEM00 mode in the image plane:

$$\text{PSF}(x, y) = (2\pi\sigma^2)^{-1/4} \exp\left(-\frac{x^2}{4\sigma^2}\right)(2\pi\sigma^2)^{-1/4} \exp\left(-\frac{y^2}{4\sigma^2}\right) \tag{20}$$

where $\sigma$ determines the width of the optical field. In our treatment, $\sigma$ is the root-mean-square radius of the Gaussian beam. It is the $1/e^2$ radius of the intensity profile and is defined in terms of the beam waist, $w_0$, as $w_0 = 2\sigma$. It is also related to the full width at half-maximum (fwhm) of the intensity profile as fwhm $= 2\sqrt{2 \ln 2}\, \sigma$). In the subsequent discussion, $\sigma$ will be used as the unit of distance, and to avoid confusion, SD will denote the standard deviation. Equation 20 is a very frequently used approximation in many areas of microscopy and leads to the popular "intensity PSF" in the lateral direction, which is given by the normalized, two-dimensional, Gaussian function, where the subscript $I$ denotes intensity:

$$\text{PSF}_I(x, y) = \left(\frac{1}{2\pi\sigma^2}\right) \exp\left(-\frac{x^2 + y^2}{2\sigma^2}\right) \tag{21}$$

Note that we assume symmetry in the $x$- and $y$-axes (i.e., $\sigma_x = \sigma_y = \sigma$). We also assume that the signal (light field) from any arbitrarily located point emitter along the $x$-axis can be modeled by a TEM00 mode displaced on the $x$-axis by a distance, $x_0$, from the origin. While for the sake of simplicity we assume only $x$-axis displacement, the treatment is generic and can be readily adapted for two-dimensional displacement. The spatial, transverse, amplitude profile of the field of the emitter on the image plane is given by

$$|E_S(x, y)| = \mathcal{E}_S \int_{-\infty}^{+\infty} \delta(x' - x_0)\text{PSF}(x - x', y - y')\, dx'\, dy'$$

$$= \mathcal{E}_S \text{PSF}(x - x_0, y)$$

$$= \mathcal{E}_S(2\pi\sigma^2)^{-1/2} \exp\left[-\frac{(x - x_0)^2}{4\sigma^2}\right] \exp\left(-\frac{y^2}{4\sigma^2}\right) \tag{22}$$

$\mathcal{E}_S$ is the spatially independent field amplitude, which is related to the overall brightness, or the number of photons representing the field of the point source. The primed and unprimed coordinates are those in the object and image planes, respectively. We did not use the primed notation for $x_0$ for the sake of simplicity, as a system with unit magnification has $x'_0 = x_0$. For a small deviation from the origin, $x_0$, it can be shown that the electric-field amplitude can be written as the linear combination of an orthonormal Hermite−Gaussian (HG) basis[38] defined with respect to the origin of the image space:

$$|E_S(x, y)| = \sum_{m=0}^{\infty} \sum_{n=0}^{\infty} c_{mn}(x_0) \text{HG}_{mn}(x, y) \tag{23}$$

where the $c_{mn}$ terms are the coefficients of the Hermite−Gaussian functions of order $(m, n)$. The first two Hermite−Gaussian functions are

$$\text{HG}_{00}(x, y) = (2\pi\sigma^2)^{-1/2} \exp\left(-\frac{x^2}{4\sigma^2}\right) \exp\left(-\frac{y^2}{4\sigma^2}\right) \tag{24}$$

and

$$\text{HG}_{10}(x, y) = (2\pi\sigma^2)^{-1/2} \frac{x}{\sigma} \exp\left(-\frac{x^2}{4\sigma^2}\right) \exp\left(-\frac{y^2}{4\sigma^2}\right) \tag{25}$$

The coefficients $c_{mn}(x_0)$ can be obtained as

$$c_{mn}(x_0) = \int_{-\infty}^{+\infty} \int_{-\infty}^{+\infty} E_S(x, y)\text{HG}_{mn}(x, y)\, dx\, dy \tag{26}$$

Therefore, a shifted PSF has a non-zero contribution of the higher-order mode, which encodes the information about shift $x_0$. If our interest is to obtain complete information about the position of the point emitter, we should, in theory, capture all of the TEM modes.[33] As we noted in the Introduction, that is not feasible. We can, however, capture a few higher-order modes (or even, more simply, just one) to extract information about the parameters. In that spirit, we shall assume that the signal field shown in eq 23 is mixed with a local oscillator field prepared in the TEM10 mode. Because of the orthogonality of the HG basis functions, this mixing will extract the TEM10 contribution from $E_S$.

The heterodyning experiment described above is designed specifically to perform this extraction. That is, the experiment determines the degree of overlap between the LO and S fields through measurement of the demodulated signal amplitude given in eq 9. We now introduce the scanning parameter $\mathbf{d} = d$ (as a continuous, single parameter), which is the shift of the local oscillator with respect to the origin of the experimental coordinate system in the image plane, in the equation for the local oscillator in TEM10. Then the transverse, amplitude profile of the local oscillator is given by

$$|E_{LO}(x, y)| = \mathcal{E}_{LO}(2\pi\sigma^2)^{-1/4} \frac{x - d}{\sigma} \exp\left[-\frac{(x - d)^2}{4\sigma^2}\right]$$

$$\times (2\pi\sigma^2)^{-1/4} \exp\left(-\frac{y^2}{4\sigma^2}\right) \tag{27}$$

$\mathcal{E}_{LO}$ is the spatially independent field amplitude of the local oscillator, which is related to the overall brightness or the number of photons representing the local oscillator. The measured signal is, therefore, proportional to the expansion coefficient, $c_{10}(x_0)$. We assume the scale of the displacement in the image plane is the same as that in the object plane and, without loss of generality, take the magnification of the optical system to be unity. Now using eqs 9, 22, and 27, we arrive at the expression for the model of the demodulated signal amplitude as

$$v(d|x_0) = 2\kappa(N_S N_{LO})^{1/2} \left(\frac{x_0 - d}{2\sigma}\right) \exp\left[-\frac{(x_0 - d)^2}{8\sigma^2}\right] \tag{28}$$

where $N_S = \mathcal{E}_S^2$ and $N_{LO} = \mathcal{E}_{LO}^2$. If we set the local oscillator to the TEM00 mode to extract the lowest-order-mode contribution of the signal field, then eqs 27 and 28 become

$$|E_{LO}(x, y)| = \mathcal{E}_{LO}(2\pi\sigma^2)^{-1/4} \exp\left[-\frac{(x - d)^2}{4\sigma^2}\right](2\pi\sigma^2)^{-1/4}$$

$$\exp\left(-\frac{y^2}{4\sigma^2}\right) \tag{29}$$

and

$$v(d|x_0) = 2\kappa(N_S N_{LO})^{1/2} \exp\left[-\frac{(x_0 - d)^2}{8\sigma^2}\right] \tag{30}$$

**Modeling Two Emitters: Double Slits as a Model Case.** While localization of a single emitter is important in single-molecule microscopy, we are often more interested in
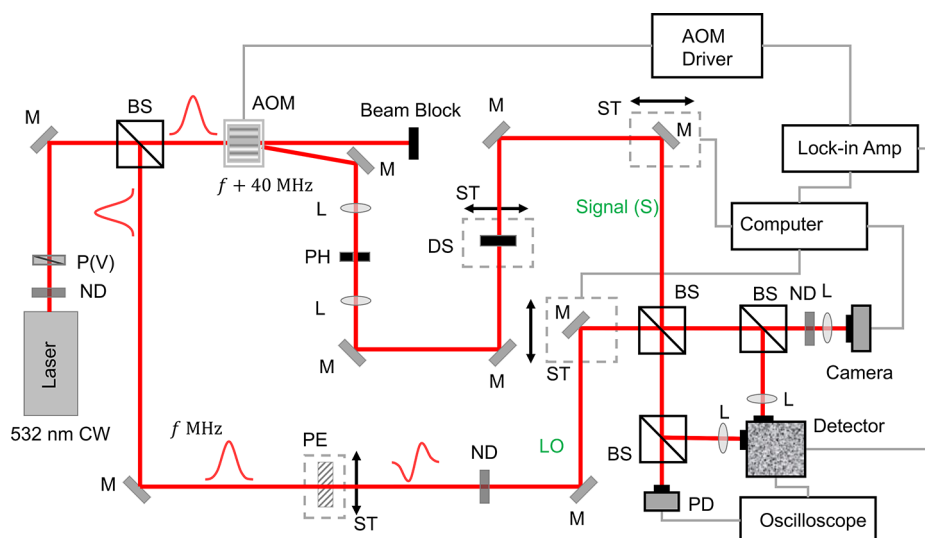
**Figure 2.** Schematic of the balanced heterodyning experiment. A 532 nm cw laser beam is polarized vertically by P and is divided by a 50:50 beam splitter (BS). The upper arm is the signal (S), a TEM00 beam modulated at 40 MHz with an AOM. Its position, $x_d$, is adjusted with a stage (ST). The lower arm acts as the local oscillator, LO, and is converted into a TEM10 beam by a passive phase element, PE. (When it is necessary to switch the LO to the TEM00 mode, this is accomplished by translating PE such that the beam passes through the constant phase area.) The profile of the LO in TEM10 is provided in Figure 3a. S and LO are combined at the second BS. The phase of LO is changed by 180° upon reflection at the BS. Abbreviations: ND, neutral density; PD, photodiode; L, lens; M, mirror. Scanning LO through S yields a voltage vs position curve. For the two-emitter case, a double slit is placed after the spatial filter to simulate the signal from two emitters. Each slit has a width $w_x$ of 150 $\mu$m and a length $w_y$ of $25 \times 10^3$ $\mu$m. Four slit separations, $x_d$, are investigated. In the upper arm, the distance from the double slits to the BS is $z = 0.80 \times 10^6$ $\mu$m. In the lower arm, the distance from the PE to the BS is $z = 1.08 \times 10^6$ $\mu$m.

localizing two or more closely spaced emitters. To determine the separation, $x_d$, of a pair of emitters, we use a procedure similar to that for localizing one. In principle, we could have approached this problem by splitting the signal beam in two and following the same steps as described above. In practice, it is nontrivial to determine the center-to-center distance of the two laser beams obtained in this manner with enough precision to be useful for the purposes of our discussion. We thus modeled two coherent point emitters with a double-slit diffraction field as the source. We take the signal as the TEM00 mode of the laser beam transmitted through double slits, whose center-to-center separation distance along the $x$-direction is $x_d$. The time-independent field of the signal beam, before it encounters the slits, is given by the PSF of eq 24 with an additional phase factor that will be necessary to account for the curvature of its wavefront in the subsequent analysis:

$$E'_S(x', y') = \mathcal{E}_S HG_{00}(x', y') \exp\left[\frac{i\pi(x'^2 + y'^2)}{\lambda R_S(z_0)}\right] \quad (31)$$

where $\lambda$ is the wavelength of the light and $R_S(z_0)$ is the radius of curvature of the input beam at the double-slit window ($z_0$ acts as a reference point). The amplitude transmittance function of the two rectangular slits is[44]

$$t_S(x', y') = \left\{ \text{rect}\left[\frac{x' - \left(\frac{x_d}{2} + c\right)}{w_x}\right] \right.$$

$$\left. + \text{rect}\left[\frac{x' - \left(-\frac{x_d}{2} + c\right)}{w_x}\right] \right\} \text{rect}\left(\frac{y'}{w_y}\right) \quad (32)$$

where $w_x$ and $w_y$ are the widths of the slits in the $x$- and $y$-directions, respectively. The rectangular function, rect($x$), has a

value of 1 when $|x| < 1/2$ and 0 elsewhere. The diffraction pattern is sensitive to the alignment of the laser beam with respect to the slits. Thus, in addition to accounting for the curvature of its wavefront, we introduce an "alignment parameter", $c$, that accounts for its unequal transmission through the slits. Then the complex signal-field distribution across the slits becomes

$$E_S(x', y') = E'_S(x', y')t_S(x', y')$$

$$= \mathcal{E}_S HG_{00}(x', y') \exp\left[\frac{i\pi(x'^2 + y'^2)}{\lambda R_S(z_0)}\right] t_S(x', y') \quad (33)$$

The time-independent field at the distance, $z_S$, after the double-slit window can be obtained from the Fresnel approximation[44,45] of the diffraction equation:

$$E_S(x, y) = \frac{e^{ikz_S}e^{\frac{i\pi}{\lambda z_S}(x^2+y^2)}}{i\lambda z_S} \int\int E_S(x', y')e^{\frac{i\pi}{\lambda z_S}(x'^2+y'^2)}$$

$$e^{-i2\pi(f_x x' + f_y y')} \, dx' \, dy'$$

$$= \frac{e^{ikz_S}e^{\frac{i\pi}{\lambda z_S}(x^2+y^2)}}{i\lambda z_S} \text{FT}[E_S(x', y')e^{\frac{i\pi}{\lambda z_S}(x'^2+y'^2)}] \quad (34)$$

$f_x$ and $f_y$ are the spatial frequencies, $x/\lambda z_S$ and $y/\lambda z_S$, respectively. FT denotes the Fourier transform.

In our experiment, the LO is converted into a TEM10 mode by transmitting a part of the laser beam in the TEM00 mode through a passive phase plate. The coating of the phase plate is such that it induces an extra $\pi$ phase shift on one side of the beam along the $x$-axis (horizontal). Thus, the transmittance function of the phase plate is
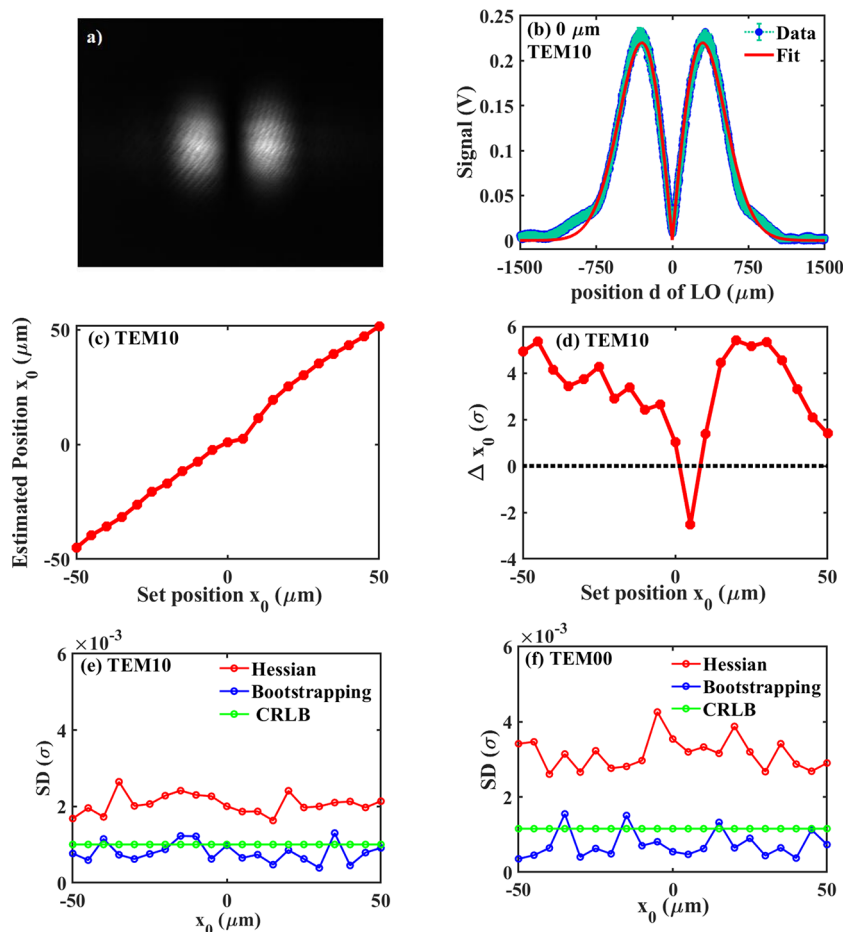
**Figure 3.** (a) Image of the LO in the TEM10 mode taken with a CMOS camera. (b) Voltage obtained from the balanced detector as the LO (in TEM10) is scanned through the S beam, which in this case is the TEM00 mode of a laser beam, which is a surrogate for a single, coherent emitter. The minimum of the signal determines its position, according to the CRLB. The position is localized to ∼0.1% of its size. (c) Estimation of the position of $x_0$ in panel b for set values of $x_0$ from −50 to 50 $\mu$m in 5 $\mu$m increments and plotted with respect to the set $x_0$ values. The positioning stage was moved both forward and backward, and the average of the estimation from the two cases was plotted to eliminate positioning bias. (d) Deviation ($\Delta x_0$) of values in panel c from the set values given in terms of $\sigma$ as a function of set $x_0$ values. This is a measure of both the estimation error and systematic bias in the optical alignment. (e) Estimated uncertainty [standard deviation (SD)] of the position of the laser beam (parameter $x_0$) obtained from the Hessian calculation during the fitting (red) and from the statistics of five measurements, i.e., bootstrapping (blue). Calculated uncertainty of parameter $x_0$ from the CRLB (green), assuming 1% uncertainty in the measured, demodulated, heterodyned signal. This analysis is for LO at TEM10. (f) Same as panel e but for LO in TEM00. The abscissa is in units of beam size, $\sigma$, for both panels e and f (the standard deviation of the position estimator, $x_0$, is the square root of the CRLB).

$$t_{\text{LO}}(x', y') = \exp\left(-i\left\{\phi_{\text{PP}} + \frac{\pi}{2}[1 - \text{sign}(x)]\right\}\right) \tag{35}$$

where $\phi_{\text{PP}}$ is an arbitrary extra phase induced due to the phase plate across its surface. The function sign($x$) is equal to 1 when $x > 0$, 0 when $x = 0$, and −1 when $x < 0$. Therefore, similar to the signal field, the local oscillator field can be written as

$$E_{\text{LO}}(x', y') = \mathcal{E}_{\text{LO}}\text{HG}_{00}(x', y') \exp\left[\frac{i\pi(x'^2 + y'^2)}{\lambda R_{\text{LO}}(z_0)}\right]t_{\text{LO}}(x', y') \tag{36}$$

where $R_{\text{LO}}(z_0)$ is the radius of curvature of the input beam at the phase plate ($z_0$ acts as a reference point). Using the Fresnel formula for the propagation of the transmitted field at a distance $z_{\text{LO}}$ from the phase plate, we obtain the time-independent field for the local oscillator:

$$E_{\text{LO}}(x, y) = \frac{e^{ikz_{\text{LO}}}e^{\frac{i\pi}{\lambda z_{\text{LO}}}(x^2+y^2)}}{i\lambda z_{\text{LO}}}\text{FT}[E_{\text{LO}}(x', y')e^{\frac{i\pi}{\lambda z_{\text{LO}}}(x'^2+y'^2)}] \tag{37}$$

In this case, the FT is evaluated at the spatial frequencies $f_x = x/\lambda z_{\text{LO}}$ and $f_y = y/\lambda z_{\text{LO}}$.

The time-dependent fields for S and LO, $E_S(x, y, t)$ and $E_{\text{LO}}(x, y, t)$, respectively, are obtained by multiplying eqs 34 and 37 by the temporal phase factors, $\exp(-i\omega_S t)$ and $\exp(-i\omega_{\text{LO}}t)$, respectively. Then, in principle, one could follow the treatment described in eqs 1−9 to obtain a model for the measured voltage. Because, however, the phase factors ($\phi$) are in general a function of the coordinates ($x, y, z$), it is nontrivial to obtain an analytical expression. Therefore, we computed them numerically. To include the scanning parameter, we substituted $x$ with $x - d_k$ in all calculations of $E_{\text{LO}}(x, y, t)$ for the scanning range given by $\mathbf{d} = (d_1, d_2, ..., d_K)$.

It is in principle possible to perform this analysis with the LO in an TEM00 mode, and for purposes of comparison, it is

useful to show the difference in performance between the LO in TEM10 and in TEM00. The form for the latter at the beam splitter is obtained by changing the transmittance function in eq 35:

$$t_{LO}(x', y') = \exp(-i\phi_{pp}) \tag{38}$$

Using procedures analogous to those discussed for the LO in TEM10, we can obtain the fields for S and LO, $E_S(x, y, t)$ and $E_{LO}(x, y, t)$, respectively, using eqs 34 and 36−38. Then the measured voltage can be computed numerically using the steps described in eqs 1−9.

## ■ EXPERIMENTAL METHODS

The apparatus for the heterodyning experiment is illustrated in Figure 2. A 532 nm continuous wave (cw) laser (Sapphire 532 SF NX, Coherent Inc., Santa Clara, CA) is split with a 50:50 nonpolarizing beam splitter (NPBS). One beam is transmitted through a passive phase element, mode converter optimized for performance at 532 nm (PE-202-Q-Y-A, Holo/OR Ltd., Ness Tziona, Israel). The passive phase element prepares the beam in a TEM10 mode, which is used as the LO. For the scanning of the LO beam across the mixing beam splitter, the mirror just before it was placed on a motorized translation stage (LNR50SEK1, with a BSC201 controller, Thorlab Inc., Newton, NJ). The laser power of the LO beam at the mixing beam splitter is typically 66 $\mu$W. The second beam, the S beam, is modulated by an AOM (AOM-402AF1, IntraAction Corp., Bellwood, IL) driven at 40 MHz (Driver ME-402, IntraAction Corp.). It is then spatially filtered to remove any distortion caused by the AOM and to provide a "clean" TEM00 beam. This beam acts as a surrogate for one point emitter. The power of the S beam is typically 37 $\mu$W before the mixing. To simulate two point emitters, a double-slit diaphragm (U14101, American 3B Scientific, Tucker, GA) with a slit width of 0.15 mm is placed after the spatial filter. In this case, the powers at the beam splitter after the double slit are typically 35, 35, 24, and 13 $\mu$W for slit separations ($x_d$) of 250, 500, 750, and 1000 $\mu$m, respectively. (The larger the separation between the two slits, the smaller the power transmitted, as more of the S beam is directly blocked.) The power for the LO in this experiment is set to 448 $\mu$W before mixing. The S beam is also placed on a motorized translation stage (UTM25PP.1, with an MM3000 motion controller, Newport Corp., Irvine, CA) before the mixing beam splitter for fine adjustment and for setting the reference point in the one-emitter experiment. The modified beams are combined at another 50:50 NPBS for mixing, as indicated in more detail in Figure 1. The mixed signals are diverted by two 90:10 reflecting, transmitting NPBSs and collected at the active surfaces of the photodiodes of a balanced photoreceiver (custom-built, SDX138, Ultrafast Sensors, Westminster, CO) by two 75 mm lenses. The active area of each photodiode has a diameter of 5 mm. The circuit of the photoreceiver has a cutoff frequency of 50 MHz. The remaining 10% of the transmitted light is used either to acquire images of the beams with a CMOS camera (DCC3240N, Thorlab Inc.) or to monitor the mixing of the two beams with another PD. The photocurrent due to the difference in the number of photoelectrons generated on each photodiode is converted to a measurable voltage by a transimpedance amplifier. The amplified voltage is measured by a lock-in amplifier (HF2LI, Zurich Instrument, Zurich, Switzerland) at 40 MHz. A dc cutoff filter (EF500,

Thorlab Inc.) and a bandpass filter (centered at 40 MHz, Minicircuit, Brooklyn, NY) are used to remove unwanted signal. The output of the lock-in amplifier is interfaced with a computer via a data acquisition card (PCIe-6353, X-series, National Instrument, Austin, TX). The data acquisition and controlling of translation stages are performed in MATLAB.

## ■ RESULTS AND DISCUSSION

**Localization of One Emitter.** Our proof-of-principle experimental demonstration employs a laser beam as a surrogate for the molecular-sized single emitter. The laser beam in TEM00 mode has a finite width defined by $\sigma$. This finite width of the beam acts as a width of the PSF in an optical imaging system. The LO (in either TEM10 or TEM00) is mixed with the "single-emitter" S beam. Figure 3b presents the experimental data for the demodulated, heterodyned signal amplitude as a function of the scanning position of the LO set in the TEM10 mode. These data are fit to the model given by eq 28. The agreement between the experimental data and the model is excellent and justifies the effectiveness of our model. It is crucial, however, to provide a rigorous analysis of the uncertainty associated with the localization of S. This was done in three ways; the results are summarized in Table 1 and Figure 3.

**Table 1. Uncertainty in $x_0$ for a Single Emitter**

| method | SD, TEM10 | SD, TEM00 |
|---|---|---|
| Hessian | $\sim 2.1 \times 10^{-3}\sigma$ | $\sim 3.1 \times 10^{-3}\sigma$ |
| bootstrapping | $\sim 0.8 \times 10^{-3}\sigma$ | $\sim 0.7 \times 10^{-3}\sigma$ |
| CLRB | $\sim 1.0 \times 10^{-3}\sigma$ | $\sim 1.2 \times 10^{-3}\sigma$ |

First, because the position of S is arbitrary unless specified in the context of the absolute laboratory frame of reference, we set a relative $x_0 = 0$ with respect to the LO. Therefore, to test the true effectiveness of the model, we must estimate $x_0$ for at least one more value of $x_0$ displaced relative to the initial reference point, "set points". We thus obtained experimental data for set points of $x_0$ ranging from −50 to 50 $\mu$m with a step size of 5 $\mu$m, to determine the effect of both the directional bias ("left" or "right") and the magnitude of this bias with a large deviation of S with respect to the optical axis on the fitting and the method of analysis. For each set point, the fitting yields an estimated value of $x_0$, whose uncertainty is obtained from a Hessian calculation. Panels c and d of Figure 3 present the estimated values of $x_0$ and their uncertainties as a function of the values of the set points. Note that the scale of deviation $\Delta x_0$ is measured in units of $\sigma$, the width parameter that is obtained from the fit of the experimental data. Second, to provide another estimation of the uncertainty of $x_0$, we also analyzed five data sets for each set position and calculated the standard deviation (SD) using a "bootstrapping" method to estimate the uncertainty.

Finally, as noted above, the CRLB sets a lower bound on the variance of any unbiased estimator of a parameter of a probability distribution. It is essential, therefore, to compute the CRLB for the variance in $x_0$ insofar as it provides a check on the precision of the heterodyning experiment to localize S and, *a fortiori*, a check on the ability of the bootstrapping and Hessian methods to estimate the uncertainty in the local-ization. It also confirms the robustness of our experimental and computational methods, as the errors provided by boot-strapping or Hessians cannot be inferior to those obtained by
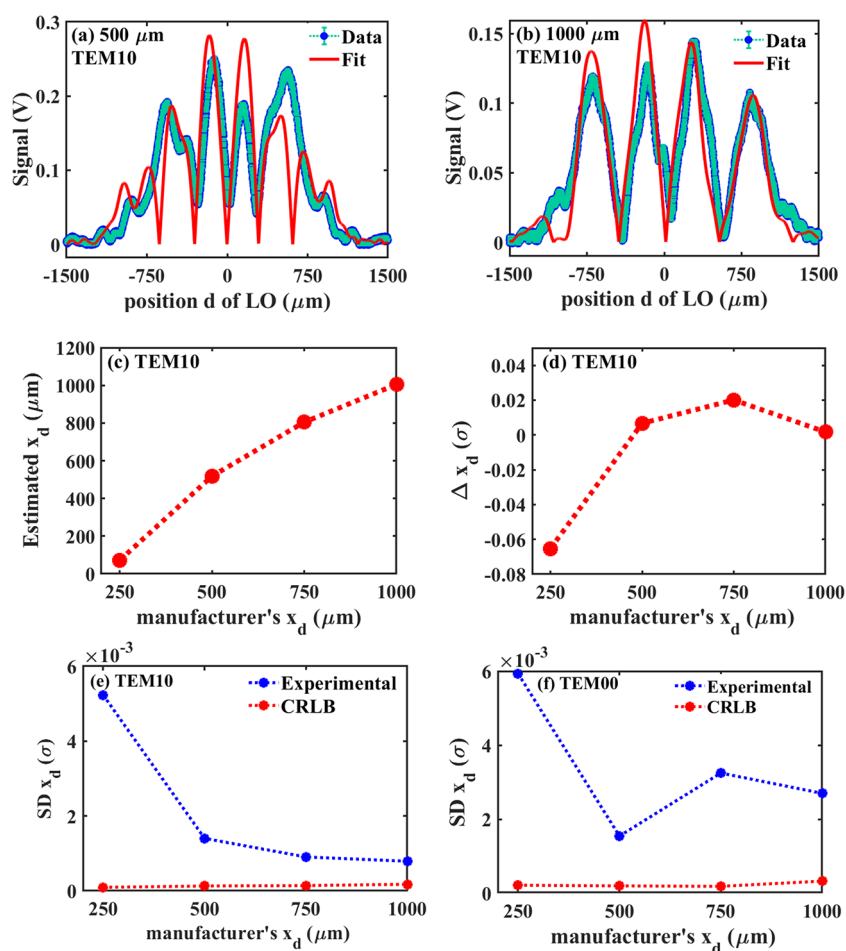
**Figure 4.** Magnitude of the output signal from the matched detector (Figure 2) as a function of scanning the LO field a distance, $d$, through the S field. The matched detector measures a voltage arising from the interference of the LO (in TEM10) with the diffracted field of S with two slits separated by (a) 500 $\mu$m and (b) 1000 $\mu$m. (c) Estimation of the separation $x_d$ for double slits with known separations (i.e., the manufacturer's $x_d$) of 250, 500, 750, and 1000 $\mu$m. (d) Deviations ($\Delta x_d$) of the values in panel c from the manufacturer's values, given in terms of $\sigma_{DS}$. (e) Estimated uncertainty [standard deviation (SD)] of the $x_d$ obtained from the statistics of five measurements, i.e., bootstrapping of experimental data (blue) and theoretical CRLB (red). This analysis is done for LO at TEM10. (f) Same as panel e but for LO in TEM00. The abscissa is in units of the beam size, $\sigma_{DS}$, for both panels e and f. The dotted lines in panels c−f serve only to guide the eye.

the CRLB. Under some reasonable assumptions, the CRLB for $x_0$ in this experiment can be calculated analytically. In this case, S is a beam with $\sigma = 150$ $\mu$m at the beam splitter, as obtained from fitting the experimental data. We considered only Gaussian noise for this analysis. The magnitude of the uncertainty in the Gaussian noise is given by the variance $\sigma_k^2$ for scan position $d_k$. As the fluctuations in the stability of our apparatus were ~1% over a time equivalent to perform the experiment, we assumed $\sigma_k$ to be 1% of the quantity $2\kappa(N_S N_{LO})^{1/2}$, which is present in both eqs 28 and 30 and independent of $d_k$. This provided the practical benefit of eliminating the need to know the values of $2\kappa(N_S N_{LO})^{1/2}$ for the computation of the CRLB. [The assumption that $\sigma_k = 1\%$ of $2\kappa(N_S N_{LO})^{1/2}$ is consistent with the experimentally measured uncertainty of the demodulated voltage signal, shown as error bars on the data points in Figure 3b.] Despite its simplicity, this CRLB calculation yields excellent agreement with the experimental results and provides considerable insight into the method for finding the position, $x_0$, of a single emitter. In the course of this discussion, it is important to keep in mind that $\sigma$ defines the beam size (i.e., the size of S) and that units

of displacement are given in terms of $\sigma$. The standard deviation is denoted by SD.

$\sigma$ characterizes the diameter of S and is 150 $\mu$m in this example. The standard deviation of the determination of the position of S, $x_0$, is given in units of $\sigma$. SDs presented in the table are the computed SDs averaged over the 21 computations for set points of $x_0$ ranging from −50 to 50 $\mu$m with a step size of 5 $\mu$m. The results are presented for the LO in TEM10 (Figure 3e) and TEM00 (Figure 3f).

There are several conclusions to be drawn from Table 1 and Figure 3. For a single emitter, the theoretical uncertainty is a bit lower for the LO in TEM10 than for the LO in TEM00. This is reasonable, as TEM10 provides more information about the displacement of S. The bootstrapping method provides an estimate of the error that is closer to the CRLB than that using Hessians and which oscillates reasonably about the CRLB. The standard deviations computed by all three methods are extremely small. This analysis confirms that the CRLB, computed under these assumptions, provides a rigorous means of predicting the limit of accuracy of localizing S before performing the heterodyning experiment. Finally, and most importantly, this analysis indicates that a nonblinking, coherent, single emitter can be localized with a precision

**Table 2. Uncertainty in $x_d$ for "Two Emitters", LO in TEM10[a]**

| method | $x_d$ = 250 $\mu$m, SD | $x_d$ = 500 $\mu$m, SD | $x_d$ = 750 $\mu$m, SD | $x_d$ = 1000 $\mu$m, SD |
|---|---|---|---|---|
| bootstrapping | $5.2 \times 10^{-3}\sigma_{DS}$ | $1.4 \times 10^{-3}\sigma_{DS}$ | $0.9 \times 10^{-3}\sigma_{DS}$ | $0.8 \times 10^{-3}\sigma_{DS}$ |
| CRLB | $9.3 \times 10^{-4}\sigma_{DS}$ | $1.3 \times 10^{-4}\sigma_{DS}$ | $1.4 \times 10^{-4}\sigma_{DS}$ | $1.7 \times 10^{-4}\sigma_{DS}$ |

[a]Unlike the case for one emitter, simplifying assumptions cannot be made here to compute the CRLB analytically. The computation is done numerically.

**Table 3. Uncertainty in $x_d$ for "Two Emitters", LO in TEM00[a]**

| method | $x_d$ = 250 $\mu$m, SD | $x_d$ = 500 $\mu$m, SD | $x_d$ = 750 $\mu$m, SD | $x_d$ = 1000 $\mu$m, SD |
|---|---|---|---|---|
| bootstrapping | $5.9 \times 10^{-3}\sigma_{DS}$ | $1.5 \times 10^{-3}\sigma_{DS}$ | $3.2 \times 10^{-3}\sigma_{DS}$ | $2.7 \times 10^{-3}\sigma_{DS}$ |
| CRLB | $2.2 \times 10^{-4}\sigma_{DS}$ | $2.0 \times 10^{-4}\sigma_{DS}$ | $1.9 \times 10^{-4}\sigma_{DS}$ | $3.3 \times 10^{-4}\sigma_{DS}$ |

[a]Unlike the case for one emitter, simplifying assumptions cannot be made here to compute the CRLB analytically. The computation is done numerically.

within 2−3 orders of the size of the laser beam, or the size of the PSF of the imaging system. This is the regime of super-resolution: the uncertainty in the estimation of the position is below the size of the spread of the field caused by the diffraction of light. Although there are technical challenges to achieving this level of accuracy for a real, nonblinking, molecular single emitter, these proof-of-concept experiments demonstrate the feasibility of achieving such resolution.

**Localization of Two Coherent Sources.** While the estimation of the position of a single emitter established the validity of our method very well, it is more interesting and useful to estimate the positions of more than one emitter. To this end, we have developed the procedure described above to estimate the separation of a "pair of emitters", $x_d$. This experiment is formulated to model the separation between two coherent emitters by the separation of two slits giving rise to a diffraction pattern. We considered four separations, which are given by the manufacturer as 250, 500, 750, and 1000 $\mu$m (see section B of the Supporting Information). Panels a and b of Figure 4 present the experimental data and fit for 500 and 1000 $\mu$m, respectively, when LO is in TEM10. We use the model described in the theoretical section for "two emitters" for a double-slit field. We fit the heterodyning data via a global optimization procedure for $x_d$ and an "alignment parameter", $c$, while fixing $R_S(z_0)$ to $1 \times 10^6$ $\mu$m. This last value is informed both by our rough estimate of the divergence of the nondiffracted beam (i.e., without the double-slit window) and by our initial attempts to fit the data with $R_S(z_0)$ as a parameter in the model while decreasing the scan resolution of the data. Similarly, we fixed $R_{LO}(z_0)$ to $1.48 \times 10^6$ $\mu$m for LO. Fixing $R_S(z_0)$ and $R_{LO}(z_0)$ decreases the complexity of the fitting model and consequently decreases the computation time, which permits us to use data with 1 $\mu$m scan resolution, thus improving the consistency of the estimation. The complex-structured data obtained in these experiments, along with an even more complex model, demand flexibility in the definition of the parameters in order to avoid local-minimum traps, which require the resources of enormous computational time, whose use becomes diminishingly significant for the broader goal of the endeavor. Thus, improvements in the data analysis are determined by the flexibility of the model, such as, for example, increasing the number of optimization parameters or possibly avoiding the paraxial approximation imposed by the Fresnel approximation.

Panels c and d of Figure 4 represent the estimated $x_d$ and the deviation $\Delta x_d$ from the manufacturer's value, respectively, as a function of the manufacturer's values of the slit separations.

Note that the deviation is scaled to the double-slit standard deviation ($\sigma_{DS} = 2.72 \times 10^3$ $\mu$m), the size parameter (root-mean-square radius) of the field calculated at the beam splitter location if a single slit of width 150 $\mu$m were present at the position of the double-slit window. $\sigma_{DS}$ represents the width of what would be termed "the point-spread function" in an equivalent, traditional, optical imaging system. The uncertainty estimated from the fitting analysis of five data sets (boot-strapping, similar to that of the single-emitter case) and the calculation of the standard deviation (SD) from CRLB are presented in Tables 2 and 3 and panels e and f of Figure 4 for an LO in TEM10 and TEM00, respectively. Unlike the single-emitter case, here the uncertainty cannot be computed from the Hessians owing to extensive "flat" regions in the parameter space.

Both from the theoretical calculation and from the experimental estimation, it is clear that when the local oscillator is set to the TEM10 mode it produces a smaller uncertainty in the estimation of slit separation as this mode carries more information as compared to its TEM00 counterpart. The decreasing trend of uncertainty is very similar to the incoherent imaging of blinking emitters; i.e., the error in estimation decreases as the separation between two emitters increases and diverges when the separation approaches zero.[30] We attribute this behavior to the incomplete information that is obtained from only one LO mode (i.e., TEM10 or TEM00). Full information can be captured only if information from all of the modes is obtained,[33] but as mentioned in the theory section, a higher-order mode, such as TEM10, should estimate localization better than TEM00, which is what has been observed in the experiments. The divergence of the uncertainty as the separation of the two slits approaches zero is also apparent in our CRLB calculations for several values of <250 $\mu$m (see Figure S5). We also note that for either LO, the theoretical SDs are slightly smaller than the experimental results. This is not surprising if we take into account all of the complications due to complex noise sources and the difficulty of aligning S, LO, and the slits. Overall, the CRLB calculation from a simple theoretical model confirms the robustness of the method in estimating the separation between two nonblinking emitters in the super-resolution regime. This potentially provides a tool for predicting the level of accuracy in localization experiments before actually performing an experiment to image multiple, coherent emitters. Thus, again similar to the case for the single emitter, the results from a "two-emitter" case indicate that multiemitter localization with a precision within 2−3 orders of

magnitude of the size of the PSF is possible. This resolution corresponds to the super-resolution regime for the particular system (i.e., the uncertainty of the resolution estimation is below the size of the spread of the field caused by the diffraction of light).

## CONCLUSIONS

We have discussed heterodyned detection as an alternative to conventional, direct imaging to defeat the Rayleigh or Abbe limits. Our theoretical and experimental results confirm others[33,37,38] for the localization of a point source, and although our approach is based upon previous schemes,[37,38] it suggests an alternative, albeit nascent, strategy insofar as we have successfully extended and demonstrated its use for the super-resolution estimation of the separation between two nonblinking coherent emitters. It is our goal to extend this strategy for the super-resolution of coherent imaging techniques, such as those based upon CARS and SRS.

Heterodyning detection differs from direct imaging.[29,30] In the latter, photons originating from two point sources having given point-spread functions (e.g., Gaussian distributions) are indistinguishable from a single point source when they closely overlap. Here, the Fisher information approaches zero and the uncertainty of the unbiased estimator for the separation given by the Cramér-Rao lower bound diverges. On the contrary, the optical heterodyning method permits the capture of information from higher-order modes of the electric field. If information from all of the modes is captured, the Fisher information remains relatively constant, and the Cramér-Rao lower bound does not diverge.[31−33]

In this work, we used the TEM10 and TEM00 modes as the LO in optical heterodyning experiments to obtain localization in the super-resolution regime for the position of one emitter and the separation of two emitters. In both experiments, TEM10 performed much better than TEM00, having lower uncertainly in the estimation of the desired parameter (position or separation). We show that objects with a $\sigma$ of $\sim$150 $\mu m$ can be localized to roughly 2−3 orders of magnitude of the point-spread function's size for a given optical system. It is important to stress that although one mode, TEM00 or TEM10, provides significant improvement, Tsang and co-workers have shown, via both quantum and semiclassical treatments, that the optimum Fisher information that can be extracted requires a complete orthonormal basis, such as the Hermite−Gaussian basis. In other words, for the Fisher information to remain relatively constant at any separation, all of the TEMs must be used.[31−33] It is, of course, neither possible nor practical to use all of the TEMs. We point this out both to highlight the improvement that one TEM can provide and to place into context the relative performance of TEM00 and TEM10 (Figure 4, Tables 2 and 3, and Figures S3−S5).

Most importantly, the heterodyning technique suggests a robust method of obtaining super-resolution localization of nonblinking, molecular emitters, such as those that might be encountered in a CARS experiment. In contrast, as mentioned in the Introduction, super-resolution techniques such as PALM and STORM require fluorescent labels or intrinsic fluorophores and rely on their random blinking to achieve super-resolution fluorescence imaging. Achieving nanometer, or subnanometer, spatial resolution for nonblinking coherent emitters might be considered difficult, but it should not be considered impossible. Comparable spatial resolution has been claimed and attained with fluorescence imaging.[1,5−7] The

manipulation of the electromagnetic field afforded by optical heterodyning, coupled with growing advances in the sensitivity and sampling times of detection devices along with innovative strategies exploiting the quantum nature of light,[46,47] can be expected to lead to the achievement of this goal in the near future.

## ASSOCIATED CONTENT

### Supporting Information

The Supporting Information is available free of charge at https://pubs.acs.org/doi/10.1021/acs.jpcb.0c10875.

(A) Additional theory and results (Figures S1 and S2) for the single emitter, (B) additional results for the two-emitter case (Figures S3−S6), (C) derivation of Fisher information when shot noise, background noise, and Gaussian noise are considered separately for the two photodiodes of the balanced detector, and (D) images of the double-slit fields (Figure S7) (PDF)

## AUTHOR INFORMATION

### Corresponding Authors

**Jacob W. Petrich** − Department of Chemistry, Iowa State University, Ames, Iowa 50011, United States; Ames Laboratory, U.S. Department of Energy, Ames, Iowa 50011, United States; orcid.org/0000-0001-9527-6832; Email: jwp@iastate.edu

**Xueyu Song** − Department of Chemistry, Iowa State University, Ames, Iowa 50011, United States; Ames Laboratory, U.S. Department of Energy, Ames, Iowa 50011, United States; orcid.org/0000-0001-5142-4223; Email: xsong@iastate.edu

### Authors

**Kalyan Santra** − Department of Chemistry, Iowa State University, Ames, Iowa 50011, United States; Ames Laboratory, U.S. Department of Energy, Ames, Iowa 50011, United States; orcid.org/0000-0002-2556-1889

**Viet Nguyen** − Department of Chemistry, Iowa State University, Ames, Iowa 50011, United States; Ames Laboratory, U.S. Department of Energy, Ames, Iowa 50011, United States

**Emily A. Smith** − Department of Chemistry, Iowa State University, Ames, Iowa 50011, United States; Ames Laboratory, U.S. Department of Energy, Ames, Iowa 50011, United States; orcid.org/0000-0001-7438-7808

Complete contact information is available at:
https://pubs.acs.org/10.1021/acs.jpcb.0c10875

### Notes
The authors declare no competing financial interest.

## ACKNOWLEDGMENTS

## REFERENCES

(1) Hell, S. W.; Wichmann, J. Breaking the diffraction resolution limit by stimulated emission: stimulated-emission-depletion fluorescence microscopy. *Opt. Lett.* **1994**, *19* (11), 780−782.

(2) Klar, T. A.; Hell, S. W. Subdiffraction resolution in far-field fluorescence microscopy. *Opt. Lett.* **1999**, *24* (14), 954−956.

(3) Lesoine, M. D.; Bose, S.; Petrich, J. W.; Smith, E. A. Supercontinuum stimulated emission depletion fluorescence lifetime imaging. *J. Phys. Chem. B* **2012**, *116* (27), 7821−7826.

(4) Huang, B.; Wang, W.; Bates, M.; Zhuang, X. Three-dimensional super-resolution imaging by stochastic optical reconstruction microscopy. *Science* **2008**, *319* (5864), 810−813.

(5) Rust, M. J.; Bates, M.; Zhuang, X. Sub-diffraction-limit imaging by stochastic optical reconstruction microscopy (STORM). *Nat. Methods* **2006**, *3* (10), 793−796.

(6) Badieirostami, M.; Lew, M. D.; Thompson, M. A.; Moerner, W. E. Three-dimensional localization precision of the double-helix point spread function versus astigmatism and biplane. *Appl. Phys. Lett.* **2010**, *97* (16), 161103−161103.

(7) Betzig, E.; Patterson, G. H.; Sougrat, R.; Lindwasser, O. W.; Olenych, S.; Bonifacino, J. S.; Davidson, M. W.; Lippincott-Schwartz, J.; Hess, H. F. Imaging intracellular fluorescent proteins at nanometer resolution. *Science* **2006**, *313* (5793), 1642−1645.

(8) Hess, S. T.; Girirajan, T. P.; Mason, M. D. Ultra-high resolution imaging by fluorescence photoactivation localization microscopy. *Biophys. J.* **2006**, *91* (11), 4258−4272.

(9) Gustafsson, M. G. Surpassing the lateral resolution limit by a factor of two using structured illumination microscopy. *J. Microsc.* **2000**, *198* (2), 82−87.

(10) Gustafsson, M. G. Nonlinear structured-illumination microscopy: wide-field fluorescence imaging with theoretically unlimited resolution. *Proc. Natl. Acad. Sci. U. S. A.* **2005**, *102* (37), 13081−13086.

(11) Cheng, J.-x.; Volkmer, A.; Book, L. D.; Xie, X. S. An epi-detected coherent anti-Stokes Raman scattering (E-CARS) microscope with high spectral resolution and high sensitivity. *J. Phys. Chem. B* **2001**, *105* (7), 1277−1280.

(12) Evans, C. L.; Xie, X. S. Coherent Anti-Stokes Raman Scattering Microscopy: Chemical Imaging for Biology and Medicine. *Annu. Rev. Anal. Chem.* **2008**, *1* (1), 883−909.

(13) Zumbusch, A.; Holtom, G. R.; Xie, X. S. Three-dimensional vibrational imaging by coherent anti-Stokes Raman scattering. *Phys. Rev. Lett.* **1999**, *82* (20), 4142.

(14) Freudiger, C. W.; Min, W.; Saar, B. G.; Lu, S.; Holtom, G. R.; He, C.; Tsai, J. C.; Kang, J. X.; Xie, X. S. Label-free biomedical imaging with high sensitivity by stimulated Raman scattering microscopy. *Science* **2008**, *322* (5909), 1857−1861.

(15) Saar, B. G.; Contreras-Rojas, L. R.; Xie, X. S.; Guy, R. H. Imaging drug delivery to skin with stimulated Raman scattering microscopy. *Mol. Pharmaceutics* **2011**, *8* (3), 969−975.

(16) Ayas, S.; Cinar, G.; Ozkan, A. D.; Soran, Z.; Ekiz, O.; Kocaay, D.; Tomak, A.; Toren, P.; Kaya, Y.; Tunc, I.; et al. Label-free nanometer-resolution imaging of biological architectures through surface enhanced Raman scattering. *Sci. Rep.* **2013**, *3*, 2624.

(17) Beeker, W. P.; Groß, P.; Lee, C. J.; Cleff, C.; Offerhaus, H. L.; Fallnich, C.; Herek, J. L.; Boller, K.-J. A route to sub-diffraction-limited CARS Microscopy. *Opt. Express* **2009**, *17* (25), 22632−22638.

(18) Bi, Y.; Yang, C.; Chen, Y.; Yan, S.; Yang, G.; Wu, Y.; Zhang, G.; Wang, P. Near-resonance enhanced label-free stimulated Raman scattering microscopy with spatial resolution near 130 nm. *Light: Sci. Appl.* **2018**, *7*, 81.

(19) Cleff, C.; Groß, P.; Fallnich, C.; Offerhaus, H. L.; Herek, J. L.; Kruse, K.; Beeker, W. P.; Lee, C. J.; Boller, K.-J. Stimulated-emission pumping enabling sub-diffraction-limited spatial resolution in coherent anti-Stokes Raman scattering microscopy. *Phys. Rev. A: At., Mol., Opt. Phys.* **2013**, *87* (3), 033830.

(20) Gasecka, A.; Daradich, A.; Dehez, H.; Piché, M.; Côté, D. Resolution and contrast enhancement in coherent anti-Stokes Raman-scattering microscopy. *Opt. Lett.* **2013**, *38* (21), 4510−4513.

(21) Graefe, C. T.; Punihaole, D.; Harris, C. M.; Lynch, M. J.; Leighton, R.; Frontiera, R. R. Far-Field Super-Resolution Vibrational Spectroscopy. *Anal. Chem.* **2019**, *91*, 8723.

(22) Kim, H.; Bryant, G. W.; Stranick, S. J. Superresolution four-wave mixing microscopy. *Opt. Express* **2012**, *20* (6), 6042−6051.

(23) Silva, W. R.; Graefe, C. T.; Frontiera, R. R. Toward label-free super-resolution microscopy. *ACS Photonics* **2016**, *3* (1), 79−86.

(24) Upputuri, P. K.; Wu, Z.; Gong, L.; Ong, C. K.; Wang, H. Super-resolution coherent anti-Stokes Raman scattering microscopy with photonic nanojets. *Opt. Express* **2014**, *22* (11), 12890−12899.

(25) Yonemaru, Y.; Palonpon, A. F.; Kawano, S.; Smith, N. I.; Kawata, S.; Fujita, K. Super-Spatial- and -Spectral-Resolution in Vibrational Imaging via Saturated Coherent Anti-Stokes Raman Scattering. *Phys. Rev. Appl.* **2015**, *4* (1), 014010.

(26) Singh, A. K.; Santra, K.; Song, X.; Petrich, J. W.; Smith, E. A. Spectral Narrowing Accompanies Enhanced Spatial Resolution in Saturated Coherent Anti-Stokes Raman Scattering (CARS): Comparisons of Experiment and Theory. *J. Phys. Chem. A* **2020**, *124*, 4305−4313.

(27) Bobroff, N. Position measurement with a resolution and noise-limited instrument. *Rev. Sci. Instrum.* **1986**, *57* (6), 1152−1157.

(28) Thompson, R. E.; Larson, D. R.; Webb, W. W. Precise nanometer localization analysis for individual fluorescent probes. *Biophys. J.* **2002**, *82* (5), 2775−2783.

(29) Chao, J.; Ward, E. S.; Ober, R. J. Fisher information theory for parameter estimation in single molecule microscopy: tutorial. *J. Opt. Soc. Am. A* **2016**, *33* (7), B36−B57.

(30) Ram, S.; Ward, E. S.; Ober, R. J. Beyond Rayleigh's criterion: a resolution measure with application to single-molecule microscopy. *Proc. Natl. Acad. Sci. U. S. A.* **2006**, *103* (12), 4457−4462.

(31) Tsang, M. Quantum limits to optical point-source localization. *Optica* **2015**, *2* (1), 646−653.

(32) Tsang, M. Subdiffraction incoherent optical imaging via spatial-mode demultiplexing: Semiclassical treatment. *Phys. Rev. A: At., Mol., Opt. Phys.* **2018**, *97* (2), 023830.

(33) Tsang, M.; Nair, R.; Lu, X.-M. Quantum theory of superresolution for two incoherent optical point sources. *Phys. Rev. X* **2016**, *6* (3), 031033.

(34) Paúr, M.; Stoklasa, B.; Hradil, Z.; Sánchez-Soto, L. L.; Rehacek, J. Achieving the ultimate optical resolution. *Optica* **2016**, *3* (10), 1144−1147.

(35) Tang, Z. S.; Durak, K.; Ling, A. Fault-tolerant and finite-error localization for point emitters within the diffraction limit. *Opt. Express* **2016**, *24* (19), 22004−22012.

(36) Tham, W.-K.; Ferretti, H.; Steinberg, A. M. Beating Rayleigh's curse by imaging using phase information. *Phys. Rev. Lett.* **2017**, *118* (7), 070801.

(37) Yang, F.; Tashchilina, A.; Moiseev, E. S.; Simon, C.; Lvovsky, A. I. Far-field linear optical superresolution via heterodyne detection in a higher-order local oscillator mode. *Optica* **2016**, *3* (10), 1148−1152.

(38) Hsu, M. T.; Delaubert, V.; Lam, P. K.; Bowen, W. P. Optimal optical measurement of small displacements. *J. Opt. B: Quantum Semiclassical Opt.* **2004**, *6* (12), 495.

(39) Yang, F.; Nair, R.; Tsang, M.; Simon, C.; Lvovsky, A. I. Fisher information for far-field linear optical superresolution via homodyne or heterodyne detection in a higher-order local oscillator mode. *Phys. Rev. A: At., Mol., Opt. Phys.* **2017**, *96* (6), 063829.

(40) Leonhardt, U. *Measuring the quantum state of light*; Cambridge University Press, 1997; Vol. 22.

(41) Mandel, L.; Wolf, E. *Optical coherence and quantum optics*; Cambridge University Press, 1995.

(42) Kay, S. M. *Fundamentals of statistical signal processing*; Prentice Hall PTR, 1993.

(43) Van den Bos, A. *Parameter estimation for scientists and engineers*; John Wiley & Sons, 2007.

(44) Goodman, J. W. *Introduction to Fourier optics*; Roberts and Company Publishers, 2005.

(45) Born, M.; Wolf, E. *Principles of optics*; Cambridge University Press, 1999.

(46) Anderson, M. D.; Tarrago Velez, S.; Seibold, K.; Flayac, H.; Savona, V.; Sangouard, N.; Galland, C. Two-color pump-probe

measurement of photonic quantum correlations mediated by a single phonon. *Phys. Rev. Lett.* **2018**, *120* (23), 233601.

(47) Burnham, D. C.; Weinberg, D. L. Observation of simultaneity in parametric production of optical photon pairs. *Phys. Rev. Lett.* **1970**, *25* (2), 84.